

Atomic-Level, Energy-Conversion Heat Transfer

Heat is stored in quanta of kinetic and potential energies in matter. The temperature represents the equilibrium and excited occupation (boson) of these energy conditions. Temporal and spatial temperature variations and heat transfer are associated with the kinetics of these equilibrium excitations. During energy-conversion (between electron and phonon systems), the occupancies deviate from equilibria, while holding atomic-scale, inelastic spectral energy transfer kinetics. Heat transfer physics reaches nonequilibrium energy excitations and kinetics among the principal carriers, phonon, electron (and holes and ions), fluid particle, and photon. This allows atomic-level tailoring of energetic materials and energy-conversion processes and their efficiencies. For example, modern thermal-electric harvesters have transformed broad-spectrum, high-entropy heat into a narrow spectrum of low-entropy emissions to efficiently generate thermal electricity. Phonoelectricity, in contrast, intervenes before a low-entropy population of nonequilibrium optical phonons becomes a high-entropy heat. In particular, the suggested phonovoltaic cell generates phonoelectricity by employing the nonequilibrium, low-entropy, and elevated temperature optical-phonon produced population—for example, by relaxing electrons, excited by an electric field. A phonovoltaic material has an ultranarrow electronic bandgap, such that the hot optical-phonon population can relax by producing electron-hole pairs (and power) instead of multiple acoustic phonons (and entropy). Examples of these quanta and spectral heat transfer are reviewed, contemplating a prospect for education and research in this field. [DOI: 10.1115/1.4051463]

M. Kaviany

Department of Mechanical Engineering,
University of Michigan,
Ann Arbor, MI 48109
e-mail: kaviany@umich.edu

1 Introduction

Interactions exist among the four principal energy carriers. These carriers are phonon, electron, fluid particle, and photon, in the energy-conversion processes. These conversions to/from thermal (heat) energy are categorized as bond energy, such as nuclear, chemical, physical bond and electromagnetic energy (thermoelectricity, and photons across the spectrum), and mechanical energy (friction, ultrasound, and wind) [1]. This broad coverage allows for unique and unified quantum mechanics (including computational) based treatment of the function of heat transfer in these energy conversions. These include electron-phonon, and photon-electron entity couplings, specifically in semiconductors (with equilibrium and nonequilibrium band structures). The research goal of this review is to provide examples of energy-conversion research. This is inspired by considering the atomic-level function of heat transfer, such as phonocatalysis, hot-phonon absorption in heterobarrier, phonon recycling, phonoelectricity, fission energy cascade while providing a perspective for this education and research field.

Figure 1 signifies the energy released per atom or molecule, undergoing nuclear or chemical reactions. The nuclear energy release is typical of the fission of uranium-235 when it absorbs a neutron directing hundreds of electron volts (eV). The endothermic chemical reaction is for typical hydrocarbons (order of one eV). The solar energy is also indicated, peaking around 2.5 eV and extending on both sides to infrared and ultraviolet. Traditionally, these energies were downconverted to heat, such as thermal energy, which at 1000 K is about 0.1 eV. It is then used in power cycles or process heating.

With advances in science and technology, solar energy is employed in solar photovoltaics (SPV) and chemical energy in fuel cells such as direct energy conversion to electricity. The fission energy continues to be converted to heat in thermonuclear

power plants; however, radioactive decay is employed in high-temperature thermoelectric generators. A new device (α -voltaic) was proposed to convert fission fragment energy directly to electricity [2]. Heat, as a product or side effect, is vital in energy conversion. Improving the conversion efficiency and discovering new energy-conversion devices depends on understanding and controlling their atomic level.

Conversion to thermal energy is an initial energy downconversion, most pronounced for nuclear energy. Innovations continue for direct energy conversion, with well-known SPV and EC cells and more challenging devices for fission products. No device exists to exploit the inner-orbital electrons with energies between nuclear and chemical bonds.

The energy conservation equation is central to heat transfer education and research. Macroscale thermal energy transport (conduction, convection, and radiation) and storage (transients including phase change) have dominated the heat transfer reach, though the function of energy conversion—specifically its atom-level origin—has not been sufficiently approached. This lack of atomic-level knowledge and insight prevented extending the heat transfer while initiating contributions to the modern atomic-level energy-conversion research. This science-based extension aims to continue evolving and emphasizing heat transfer education and research.

Figure 2 illustrates the heat transfer education/investigation fundamentals related to a phonon, electron, fluid particle, and photon. It starts with the quantum mechanics (ab initio) applied to the atomic structure and properties of solids and fluids, including new energy-related materials. The next scale-up is the molecular dynamics, followed by the Boltzmann (mesoscale) and macroscale approaches. Recent advances in computational quantum mechanics allowed for an extension of heat transfer research into thermoelectric materials and electron-phonon coupling. The function of quantum mechanics (ab initio treatments) is established as central to advances in heat transfer research [2–19].

The multiscale treatment of energy conversion regarded the discovery of new energy materials and energy-conversion methods and devices. The Bohr radius $r_B = 53$ pm, and the atomic time scale $\tau_a = 0.0021$ fs. N is the number of particles in molecular

Contributed by the Heat Transfer Division of ASME for publication in the JOURNAL OF HEAT TRANSFER. Manuscript received May 26, 2021; final manuscript received June 8, 2021; published online July 19, 2021. Assoc. Editor: Portonovo S. Ayyaswamy.

Direct versus Thermal Energy Conversion

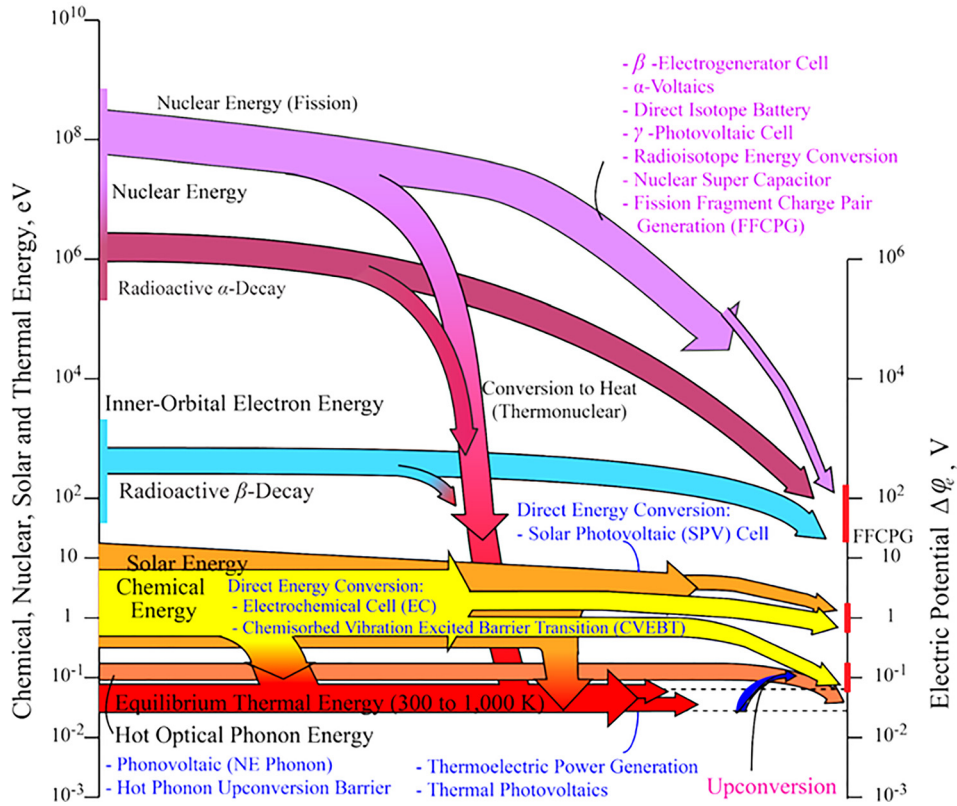


Fig. 1 Direct and thermal energy conversion of a chemical bond, nuclear (fission), and solar energy

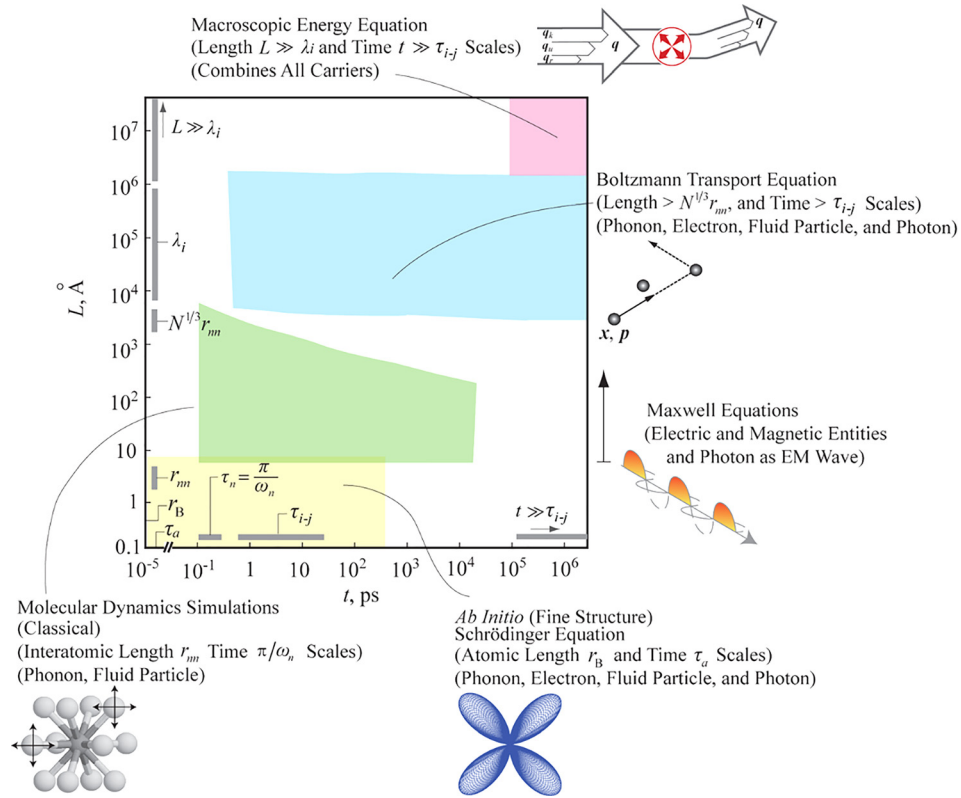


Fig. 2 The four principal energy carriers (phonon, electron, fluid particle, and photon), and four scales of treatment of energy transport, storage, and conversion [5]

dynamics simulation; λ is the mean free path; τ is the relation time and subscript; i represents one of the four carriers.

2 Atomic-Level Heat Transfer

Figure 3 indicates the emission of phonons in energy-conversion processes where the energy may be released from the chemical bond in a catalytic reaction, penetrating charged fission fragments, field-accelerated electrons, absorbed photon, or from a magnetic field in magnetic materials. These phonons are emitted directly or after an electric or magnetic excitation, followed by nonradiative decay. The intent of these processes is not to emit phonons (heat). Such emissions, therefore, are a measure of the inefficiency of energy conversion to the intended work. With attention to semiconductors, these are resonant optical phonons since the probability of emitting a single high-energy phonon is higher than emitting two or more lower-energy phonons.

An opportunity, therefore, exists to absorb these nonequilibrium (hot) optical phonons in phonon harvesting processes and devices. Under optical-phonon harvesting, they are resupplied by phonon upconversion and can also be induced by employing heterojunction where the phonons transmitted from a soft solid add to the population of low-energy phonons in harder solid. This ensures selectively adding to the upconversion rate of the native phonons. As part of the atomic-level heat transfer in energy conversion, the function was examined by reviewing phonon recycling and its conversion to electricity (as in phonovoltaics [10]). Examples commence with phonocatalysis.

Direct phonon emission can be associated with an adsorbed fluid particle, penetrating ions, accelerated electrons, absorbed photons, or a magnetic field. Indirect phonon emissions also exist by various electronic decays. Emitted phonon can be down- or upconverted before absorption. Examples of phonon harvesting are phonovoltaics tuned infrared emitter, phonocatalysis, laser

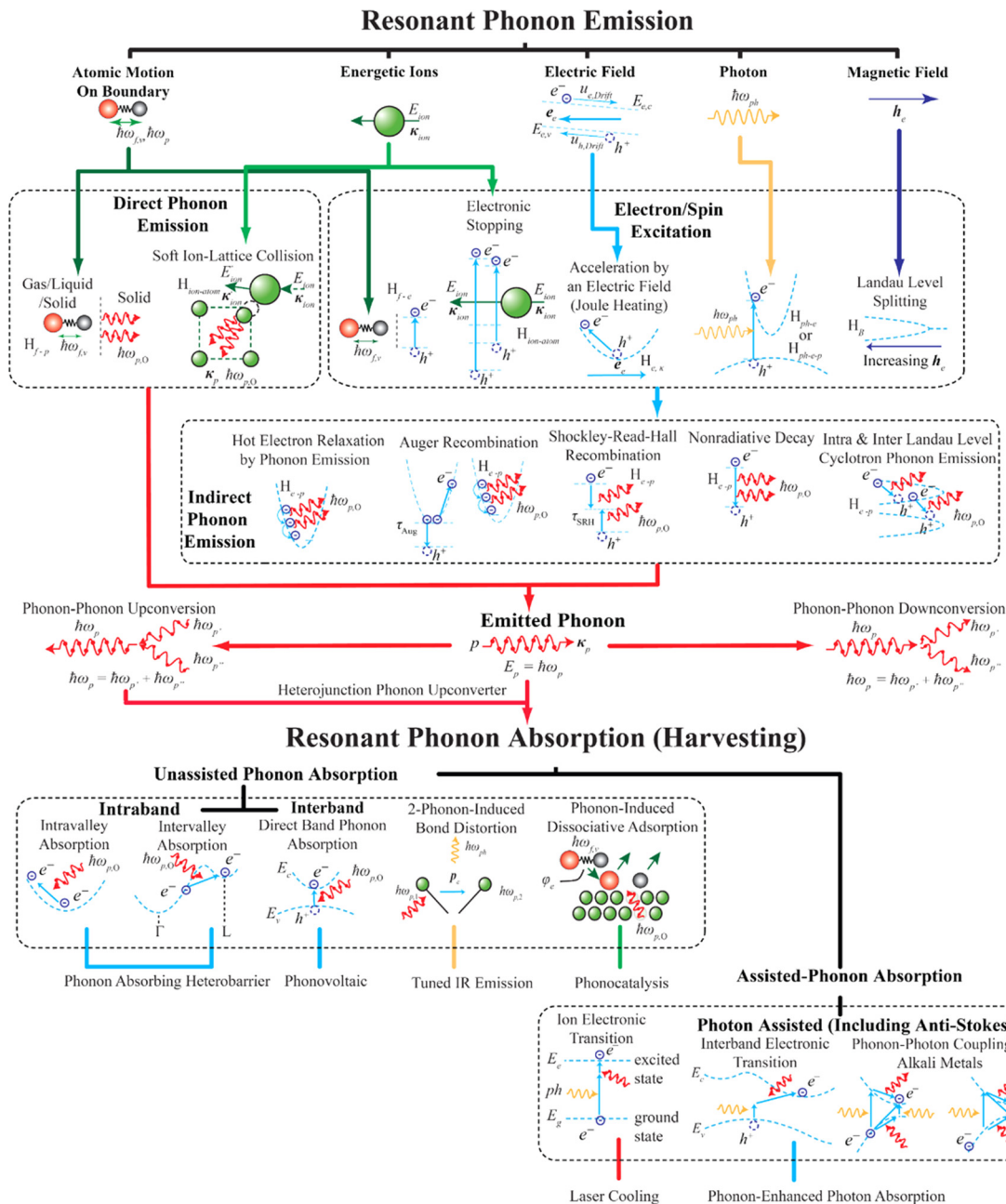


Fig. 3 Phonon emission and harvesting (absorption)

cooling, and phonon-assisted photon absorption, phonon recycling in atomic-level energy conversion. Atomic spectral heat transfer in solid-state is associated with these phonon physics phenomena.

3 Phonocatalysis: Chemisorption Dissociation With Phonon

Several advances were destined in energy conversion by employing semiconductors. The atomic-level solid-state research and thermal research, therefore, developed significantly. An example of the fluid-phase energy conversion is included. Figure 4 indicates the reaction pathway of the *phonocatalysis* that is chemisorbed dissociation of XeF₄ enabled by the boron nitride (BN) phonons only [8]. To demonstrate the controllable phonocatalysis, h-BN and XeF₆ are selected as a substrate and adsorbent; the hexagonal lattice h-BN layered structure allows for a smooth surface, weak Van Der Waals forces between layers, and a strong in-plane covalent bond (high phonon cutoff energy of 200 meV). The h-BN is a semiconductor with a large bandgap (4.0 eV) with high chemical stability; its lattice constants calculated are 2.49 Å in-plane and 6.46 Å across-plane discussions. The thin film h-BN displays low and high-energy enhancement and scattering in D_p . The results are obtained by ab initio molecular dynamics (AIMD).

The energy required to dissociate the F atom is 0.372 eV, the activation energy between the transition state (TS) and II state. Energy is released as F/BN bonds and XeF₄ are developed; the comprehensive reaction is exothermic. The activation energy for dissociating F atom is 372 meV, and there is a steep activation ascent from near ② and TS which corresponds to the energy of about 320 meV. It is expected that the gradual climbing from II to near ② can be easily achieved by absorbing plentiful 39 meV phonon energy, the acoustic phonon peak which can be seen in the BN. To complete the dissociation process, the steep ascent toward TS must be overcome by absorbing the remaining energy of 333 meV. It is also expected that this energy quantity can be provided by two-phonon contribution (two phonons of 165.5 meV) from high-energy optical phonons of BN because large-energy phonons around 150~180 meV found in BN (phonon peak at 161 meV and energy cutoff at 200 meV). The dissociation does not occur if the surface cannot provide these high-energy phonons.

TS attributable to the F atom dissociation can be seen only in the first chemisorption. This surface reaction is only facilitated by the substrate phonons—a phenomenon termed *phonocatalysis* [8].

3.1 Heavy Isotope With Lower Phonon Cutoff Energy.

The contribution of this phonon energy channel on the dissociative chemisorption is verified by controlling the substrate

phonons, indicating atomic dissociation from parent molecule controlled by phonons by employing progressively heavier isotopes of B and N atoms. With ab initio calculations, the reaction pathway and energies are assessed. Molecular dynamics simulations are implemented to demonstrate the controlled chemisorbed dissociation with spectral analysis of the surface atomic motion. Results for normal B and N atoms and 1.5 times heavier isotopes are compared.

3.2 Target B-Atoms Transient Vibration Response. The z -direction displacement-square of the B atom in Fig. 5 reflects the vibration characteristics after each event. As XeF₆ is pulled toward the surface, z -direction displacement of B-atoms becomes larger than that before the event, and the adsorption occurs on the surface. The interaction of XeF₆ with the surface is weak. The electron charge is, therefore, minor compared to that of the chemisorption. Chemisorption occurs rapidly within 32 fs, coincident to the simulation result in Ref. [8] that the time required for fluid particles approaching near-surface to exchange energy with phonons is about 35 fs. The graph becomes denser after the reaction, indicating an increase in vibration frequency. Electron density indicates that an F/h-BN bond is formed with the F and B atom attracting each other. As a product, XeF₄ is formed, desorbing after 400 fs from chemisorption. Interaction becomes extremely weak again as observed from the electron charge. The h-BN thin film with B and N heavier isotopes cannot make a reaction; XeF₆ remains adsorbed on the surface. No significant change is observed in the vibration because there is no reaction.

The initial time is shifted to the point where XeF₆ is near the surface. Regions for each event from its starting phase are shaded with diverse gray scales. XeF₆ chemisorbed on the B atom of the h-BN surface with normal atoms after adsorption; h-BN with B and N heavier isotopes, though, cannot make the reaction with the molecule [8].

Note that phonon up- and down-conversion occurs much faster and provides by [6,19,20]

$$\frac{1}{\tau_{p-p,down/up}} = \frac{\hbar}{8\pi\rho^3} \frac{|M_{p-p}|^2 R}{u_{p,A}^7 u_{p,O}^2} \omega_{p,A}^2 \omega_{p,O}^3 [f_{p,\omega_{p,A}} + 0.5 \pm 0.5]^2 [f_{p,\omega_{p,O}} + 0.5 \mp 0.5]$$

$$|M_{p-p}|^2 = 4\rho^2 \gamma_G^2 u_{p,A}^2 u_{p,O}^2, \quad R = \frac{2}{32} \frac{\Gamma_{NN} - \Gamma_{BB}}{\Gamma_{NN} + \Gamma_{BB}}$$

$$\frac{1}{u_{p,A}} = \frac{1}{u_{p,A,L}} + \frac{2}{u_{p,A,T}}, \quad f_{p,\omega} = \frac{1}{e^{\frac{\hbar\omega}{k_B T}} - 1} \quad (1)$$

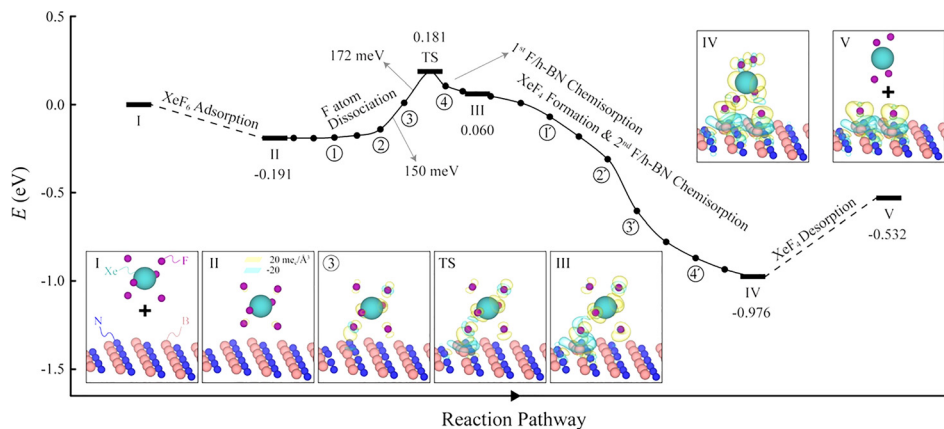


Fig. 4 Ab initio molecular dynamic prediction of reaction pathway for XeF₆ adsorption, F/BN chemisorption, and XeF₄ desorption, with snapshots with distributions of charge density difference [10]. Copyright 2016 by American Institute of Physics.

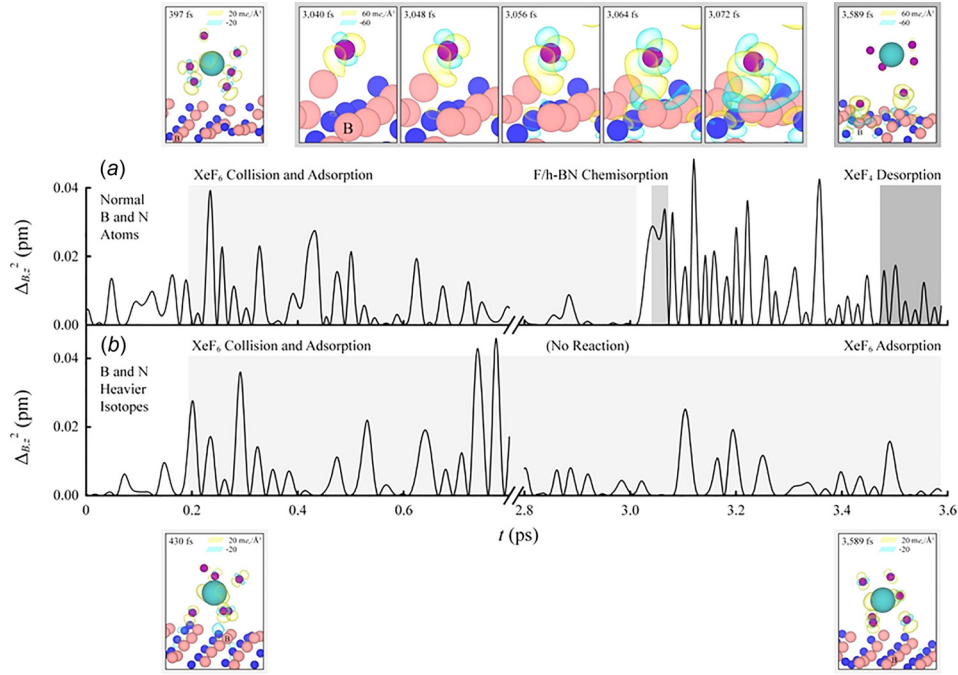


Fig. 5 The z-direction displacement-square of B atom obtained by AIMD calculation with snapshots with a distribution of electron density difference for (a) normal B and N atoms and (b) B and N heavier isotopes [10]. Copyright 2016 by American Institute of Physics.

where $u_{p,A/O}$ is acoustic/optical phonon speeds, $\omega_{p,A/O}$ is acoustic/optical phonon frequencies, $f_{p,\omega}$ is equilibrium phonon occupancy, Γ_{NN} is the force constant for N – N, and γ_G is the Grüneisen parameter. With $\rho = 2279 \text{ kg/m}^3$, $u_{p,AL} = 13.6 \times 10^3 \text{ m/s}$, $u_{p,AT} = 5.34 \times 10^3 \text{ m/s}$, $\gamma_G = 0.1$, $\Gamma_{NN} = 771.2 \text{ N/m}$,

$\Gamma_{BB} = 354.9 \text{ N/m}$ [4,21–23], and with $\hbar\omega_{p,A}$ and $\hbar\omega_{p,O}$ of 39 and 78 meV, respectively, the phonon up- and downconversion $\tau_{p-p} = 0.047 \text{ ps}$, and for $\hbar\omega_{p,A} = 95$ and $\hbar\omega_{p,O} = 190 \text{ meV}$, it is $\tau_{p-p} = 0.015 \text{ ps}$. So, the phonon energy occupancy is at near equilibrium in the phonocatalysis processes.

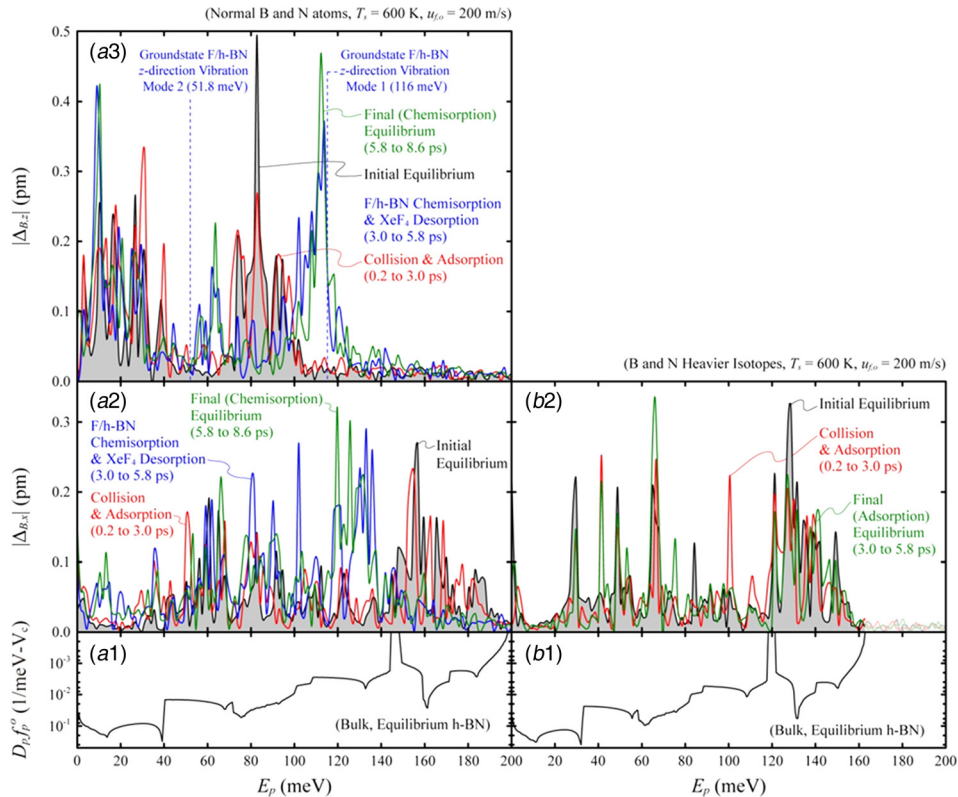


Fig. 6 Transient spectral analysis of displacement of targeted B (a) for normal B and N, and (b) for heavier isotopes [10]. Copyright 2016 by American Institute of Physics.

3.3 Phonon Energy Transfer Channels. Figure 6 indicates the transient spectral analysis for the displacement of B atom from AIMD result and comparison with phonon population for bulk h-BN at equilibrium for (a) normal h-BN and (b) B and N heavier isotopes. (1) Phonon population, (2) fast Fourier Transform (FFT) for x-direction, and (3) FFT for z-direction with F/h-BN z-direction vibration modes. The F/h-BN chemisorption occurring by normal B and N atoms changes the distributions of phonon energies dramatically, but B and N heavier isotopes cannot trigger the reaction and phonon energy bands remain almost the same. Note that phonon energies over 163 meV do not exist in B and N heavier isotopes physically; this region is lightly shaded in (b2) attributable to the FFT limitation (noise).

(1) Phonon population, (2) FFT for the x-direction, and (3) FFT for the z-direction, with F/h-BN vibration modes are also illustrated. The F/h-BN chemisorption changes the distribution of phonons dramatically, but phonon energy bands of heavier isotopes remain almost the same. Phonon energies over 162 meV do not exist in the heavier B and N lattice [8].

The accurate ab initio simulations of phonocatalysis dynamics offer insight into the controlled chemisorbed reactions with the critical function of the optical phonons. This example indicates that the heterogeneous reaction (chemisorbed dissociation) on a large bandgap semiconductor surface can be controlled by its phonons. In the XeF₆ dissociation with the h-BN system, two high-energy phonons are absorbed to overcome the activation energy. With heavier B and N isotopes, however, the contribution of three or more low-energy phonons is necessitated for the pathway ascent, attributable to the lack of high-energy optical phonons required for the reaction by two-phonon absorption.

4 Phonon Absorption in Heterobarrier: Partial Joule Heating Reversal

4.1 Heterobarrier. In semiconductor devices, the hot-phonon absorption barrier (HPAB) employs a graded heterobarrier to recycle Joule heat. For an aluminum concentration variation in the Al_xGa_{1-x}As hot-phonon absorbing barrier heterostructure, it is

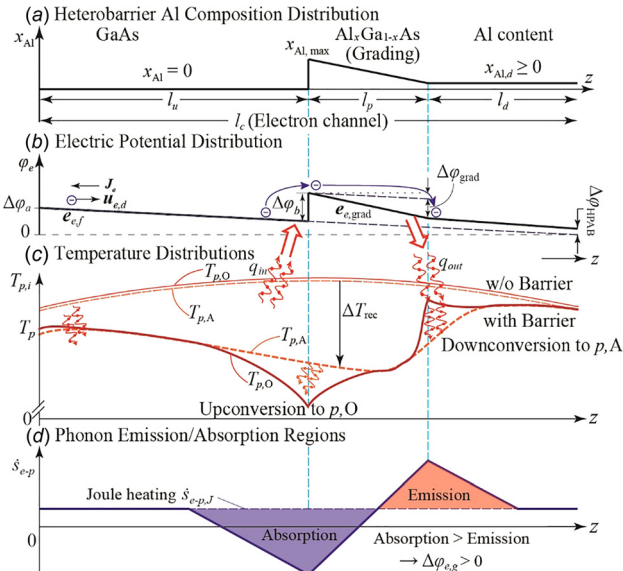


Fig. 7 (a) Aluminum concentration in the Al_xGa_{1-x}As hot-phonon absorbing barrier heterostructure; (b) the potential energy throughout an HPAB under an applied electric field $e_{e,f}$; (c) the optical and acoustic phonon temperature distribution with this heterostructure, where $T_{p,A}$ and $T_{p,O}$ are the acoustic and optical-phonon temperatures; (d) an illustration of the rate of phonon production and absorption near the barrier [19]. Copyright 2013 by American Physical Society.

indicated in Fig. 7. In the HPAB, energetic electrons flow across the heterobarrier (with potential energy $\Delta\phi_b$), cooling the electron population. A grading reaccelerates the electrons passing over the barrier, minimizing the adverse current while reducing the electrical resistance of the structure. The grading accomplishes this by inducing an electric field, e_e , on the electronic population, which causes potential energy loss; $\Delta\phi_e = e_e e_p l_p$, where l_p is the length of the graded structure. Some excess potential energy remains, $\Delta\phi_{HPA} = \Delta\phi_b - \Delta\phi_e$ such that a current flowing across the heterostructure must absorb heat to achieve this. In contrast to the thermophotovoltaic and the photon-enhanced thermionic, the HPAB focuses on the in situ cooling of a device rather than thermal electricity generation.

4.2 Hot-Phonon Absorption Efficiency. The phonon nonequilibrium arises near these barriers and manipulation of nonequilibrium optical-phonon populations, and the HPAB [16] of the first to describe such a mechanism. The efficiency of the HPAB is derived by noting that when an HPAB is inserted into a channel between the source and the drain, the phonon recycling efficiency is defined as the total heat generation within the channel as compared to the heat generation without an HPAB. Assuming that heat generation is attributable to the Joule heating, the following:

$$\eta_{HPAB} = \frac{\int_0^{l_c} (\dot{s}_j - \dot{s}_{e-p,b}) dz}{\dot{s}_j l_c} \quad (2)$$

where l_c is the length of the channel, \dot{s}_j is the Joule heating expected without the HPAB, and $\dot{s}_{e-p,b}$ is the net energy released by phonon emission within the HPAB structure. In this case, $\int_0^{l_c} (\dot{s}_j - \dot{s}_{e-p,b}) dz$ is provided by the energy required for a current flux to gain $\Delta\phi_{HPA}$ as it flows across the HPAB, the following:

$$\eta_{HPAB} = \frac{j_e \Delta\phi_{HPAB}}{\dot{s}_j l_c} = \frac{\Delta\phi_{HPAB}}{\dot{s}_j l_c / \sigma_e} \quad (3)$$

From Eq. (3), the efficiency is maximized when the current vanishes, the conductivity is high, the effective HPAB barrier height is large, and the channel is small. The assumption that the barrier does not increase the resistance between source and drain fails as the barrier. Figure 8 indicates that the thermodynamic limit to the HPAB efficiency is 40% at 300 K [16]. This occurs as the current density (and cooling power) vanishes. Ensemble Monte Carlo

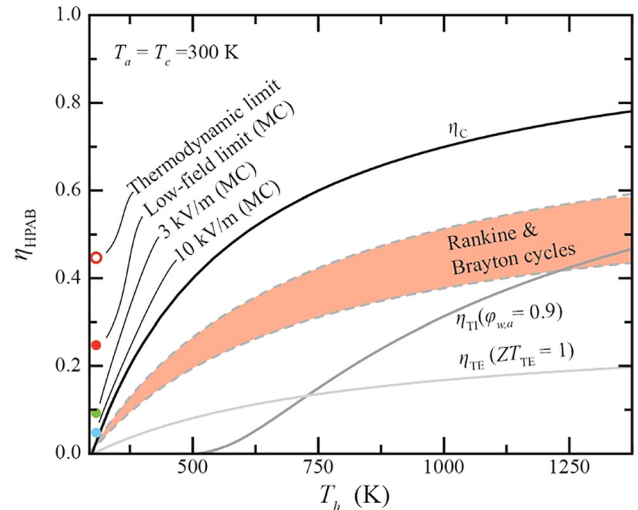


Fig. 8 The predicted efficiency of the HPAB as compared to a Carnot η_c , thermionic (TI), and thermoelectric (TE) cells [15,19]. Copyright 2013 by American Physical Society.

Boltzmann transport investigations of $\text{Al}_x\text{Ga}_{1-x}\text{As}$ HPAB achieve, at most, half of the efficiency limit. This efficiency drops rapidly as the field strength increases, as shown in Fig. 8.

While much less efficient than, for example, the thermophotovoltaic, photon-enhanced thermionic, and thermoelectric devices, the HPAB enables integrated micro- and nanoscale cooling with potentially greater efficiency than optical refrigeration. While HPABs could be integrated into a macroscale device, the heat-harvesting technologies outperform them, which work at the macroscale. At the nano- and microscales, however, HPABs do not suffer from concerns such as the electrical contact resistances. These resistances prohibit employing microthermoelectric coolers. They, therefore, find a potential niche as a nanoscale, in situ heat harvester. This device has not been realized experimentally yet. This remains the most crucial step in its evaluation as a potential cooling technology grows larger, the current density grows, and the channel length vanishes.

Monte Carlo simulations predict much lower efficiency than the thermodynamic limit [17], and the efficiency drops rapidly with the applied field strength [16].

5 Phonon Recycling: In Situ Assisted Absorption of Emitted Phonons

The perturbation theory is generally applied to rather weak interaction and more accurate, but highly involved treatment of the strong coupling [15]. The ab initio approach is developed to determine the photon-electron and electron-vibration coupling rates for ion-doped materials related to laser cooling of solids. The ground and excited state energies are determined, and the corresponding geometries are optimized. Employing the first-principle wave functions, the electric transition dipole moment connecting the ground and excited states are calculated, established as highly dependent on the symmetry properties of the system. The electron-phonon coupling is caused by the modification of the electronic wavefunction in response to the nuclei motions and by the modifications of the vibrational modes before and after the transition. This theory is employed to calculate the nonradiative decay rate, strongly dependent on the temperature.

In ion-doped lasers, phonons are emitted in the lasing layer by temperature-independent rapid single-phonon decay and by temperature-dependent multiphonon decay. These nonequilibrium phonon distribution propel phonon propagation to the adjacent cooling layer. The propagation process involves acoustic-optical-phonon up- and down-conversion, three-phonon processes, and optical and acoustic phonon transmission, influenced by the phonon spectrum of both layers [19,20]. The reuse of nonequilibrium phonons (heat) emitted from the energy conversion through various phonon absorption processes reduces required external cooling. Figure 9 schematically confirms this motion.

The input and output energy paths are indicated by the light gray arrows, whereas the phonon energy path is demonstrated in a dissimilar shade. The photon, electron, and phonon energy-conversion regimes are labeled. The carrier couplings are also signified.

5.1 Phonon Recycling in Ion-Doped Laser Layer and Its Adjacent Cooling Layers. Phonon emission is an energy-conversion efficiency loss in photonic transition processes. Phonon recycling by the anti-Stokes fluorescence cooling results in a lower operating temperature. Transmitted optical phonons cross a heterogeneous boundary. The upconverted acoustic phonons contribute to higher occupancy of the optical phonon while increasing the second-order transition rate. Phonon spectra optimization renders upconversion favorable. Here, a theoretical study and quantitative efficiency results for phonon recycling in Yb^{3+} doped yttria-alumina garnet lasing layer and its adjacent Yb^{3+} : ZrF_2 cooling layers are reviewed [6]. Figure 10 presents a schematic presentation of these results.

The energy flow diagram with carrier interactions for the ion site photon and phonon energy is demonstrated. The cooling layer has a higher phonon cutoff frequency, which facilitates the cooling rate [6].

5.2 Fermi Golden Rule for Weak Photon-Electron-Phonon Interaction. The Hamiltonian for the physical system for the phonon-assisted photon absorption process is (e stands for electronic, p for phononic, and ph for photonic) [5–7]

$$H_e + H_p + H_{ph} + H_{ph-e} + H_{e-p} \quad (4)$$

The second-order (weak) transition process is treated by employing the Fermi golden rule approach; the final form of the transition (phonon absorption or cooling) rate is

$$\dot{s}_{ph-e-p} = \left(1 - \frac{\bar{\omega}_{ph,e}}{\omega_{ph,i}} \eta_{e-ph}\right) \hbar \omega_{ph,i} \frac{\pi \hbar}{2m} \frac{(s_{ph,i} \cdot \mu_{ph-e})^2 D_p(E_p) f_p^o(E_p) L}{\epsilon_0 E_p^3 u_{ph} n_{d,c} V} \quad (5)$$

where m is the reduced mass of the host atomic pair; $s_{ph,i}$ the polarization vector; μ_{ph-e} is electronic transition dipole moment vector; $\phi'_{e-p;O}$ is optical-phonon deformation potential; $D_p(E_p)$ is phonon density of state of phonon having energy E_p ; f_p^o is the equilibrium boson distribution function; L is photon transit length; u_{ph} is the speed of light; and $(Q_{ph,p} - Q_{ph,a})/n_{d,c} V$ represents photon intensity per ion. The phonon-assisted photon transition rate, therefore, is a function of atomic properties of the dopant ion and host, optimized for desired performance.

5.3 Phonon Recycling Efficiency. Figure 11(a) indicates the cooling efficiency heat removed by the anti-Stokes cooling/total heat generated by lasing as a function of temperature [6]. The results are for three diverse cooling crystals (ZrF_2 , CdF_2 , and WF_2) with dopant Yb^{3+} , and Yb^{3+} : yttria-alumina garnet (Yb^{3+} : YAG) as lasing crystal. The cooling crystal hosts are selected for their high, moderate, and low peak phonon energies. The method for evaluating the atomic quantities is given in Eq. (3). With Yb^{3+} : ZrF_2 cooling layer, anti-Stokes's cooling removes 30% of the generated heat (phonon emission by nonradiative decay). Employing low phonon cutoff material (CdF_2) results in low optical-phonon transmission and upconversion. Employing high phonon cutoff material (WF_2) results in a low phonon-assisted absorption rate attributable to a large molecular mass and a small phonon occupation number. Figure 11(b) signifies the reduced heating, such as the laser crystal operating 12 K lower compared to nonrecycled, requiring 35% less crystal cooling.

6 Photoelectricity: Creating Electron-Hole Pair With Phonon Energy

6.1 The Efficiency and Figure of Merit of the Phonovoltaic Cell. Figure 12 indicates the phonovoltaic cell is an example of photoelectricity [10–12], harvesting optical phonons equivalent to how a photovoltaic harvests photon. It implies a nonequilibrium (hot) population of optical phonons more energetic than the electronic bandgap ($E_{p,O} > \Delta E_{e,g}$) relaxes by generating electron-hole pairs in a diode (a p - n junction). This splits them to produce a photoelectric current, voltage, and power. This must occur faster than the hot optical-phonon population down-converts into the acoustic phonon modes, producing heat rather than electricity. When the phonovoltaic cell becomes sufficiently larger than the electrons and acoustic phonons, it produces and accumulates, inhibiting generation and downconversion. This drastically reduces the local nonequilibria while enhancing the spatial nonequilibrium. The local nonequilibrium vanishes in the long length limit. If the contacts are maintained at a cold temperature, T_c , and

the active junction reaches a hot temperature, T_h , then the spin Seebeck effect induces a current, and/or forms an electric potential ($\alpha_S \Delta T$). This is attributable to the temperature gradient.

Generation events in the p - n junction supply this current and maintain the quasi-equilibrium condition; however, the generated electrons equilibrate with their surrounding environment before collection. They will not remove heat equal to the bandgap or optical-phonon energy. Instead, they will remove the Peltier heat, $Q_P = J_e \alpha_S \Delta T$. This implies a macroscale phonovoltaic generates thermoelectricity (and thermal electricity) in a device termed the thermovoltaic cell. The phonovoltaic can, therefore, trace its history. Span et al. [24] proposed the thermovoltaic cell as a variation on the thermoelectric cell. The advantage they observed in the thermovoltaic was its removal of the p -metal- n junction and the associated contact resistances at the hot side of the thermoelectric generator. The notion to employ a nanoscale device to exploit the local nonequilibrium between the optical phonons and electrons did not arrive until 2016.

In the phonovoltaic, an optical-phonon source ($\dot{S}_{p,O}$) heats the optical-phonon population. This population at temperature T_h , relaxes by interacting with the cold acoustic phonon modes and electrons at temperature T_c , generating either acoustic phonons (and entropy) at rate $\dot{\gamma}_{p-p}$ or electron-hole pairs at rate $\dot{\gamma}_{e-p}$. The intrinsic electric field of a diode, such as a p - n junction, splits the electron-hole pairs, creating a current while generating power. As the electrons and hole accumulate in the diode, the quasi-Fermi levels of both populations ($E_{F,n}$ and $E_{F,p}$) shift toward their respective band edges. This creates an electric potential $\Delta\phi_a$ while inducing recombination as the excited populations (with occupation f_e and f_h) relax toward their equilibrium occupations f_e^0 and f_h^0 . When $\Delta\phi_a$ grows sufficiently large, the rate of generation balances with that of recombination [10–12].

The ratio of the power produced ($P_e = e_c J_e \Delta\phi_a$, where J_e is the current extracted across the applied potential energy $\Delta\phi_a$) to the energy supplied ($Q_{in} = E_{p,O} \dot{S}_{in}$, where \dot{S}_{in} is the rate of optical phonons generated by an arbitrary optical-phonon source), which determines the pV efficiency ($\eta_{pV} = P_e/Q_{in}$). In an ideal junction (with no excess current loss, such as that from surface recombination or junction tunneling) with negligible internal resistance, the current produced is proportional to the net generation (\dot{n}_e) within the cell volume (V), i.e., $J_e = e_c \dot{n}_e V$. The energy flow required to produce this current is $Q_e = E_{p,O} J_e$. Additional heat, however,

flows from the hot optical-phonon population into the acoustic branches attributable to the net-downconversion rate ($\dot{n}_{p,A}$) within the cell volume, indicating $Q_{p,A} = E_{p,O} \dot{n}_{p,A} V$. Assuming that the interband electron-phonon and phonon-phonon interactions dominate the optical-phonon lifetime, the controlling equations become

$$\begin{aligned}
 P_e &= J_e \Delta\phi_a = e_c \dot{n}_e V \Delta\phi_a \\
 Q_{in} &= Q_e + Q_{p,A} = E_{p,O} V (\dot{n}_e + \dot{n}_{p,A}) \\
 \eta_{pV} &= \frac{P_e}{Q_{in}} = \frac{e_c \Delta\phi_a}{E_{p,O}} \frac{\dot{n}_e}{\dot{n}_e + \dot{n}_{p,A}} \text{ phonovoltaic efficiency} \\
 \eta_{pV} &= \frac{\dot{n}_e}{\dot{n}_e + \dot{n}_{p,A}} = \dot{\gamma}_{e-p}^* \text{ quantum efficiency} \\
 Z_{pV} &= \frac{\Delta E_{e,g}}{E_{p,O}} \dot{\gamma}_{e-p} \text{ pV figure of merit}
 \end{aligned} \tag{6}$$

The relationship between the net generation and voltage is required to determine the efficiency and power output of a pV cell.

6.2 Phonovoltaic Materials. In addition to our requirement that $E_{p,O} > \Delta E_{e,g}$, the bandgap is required to be substantially larger than the thermal energy, $k_B T_c$. Otherwise, the diode will not function well; the fill factor will fall, and the generation will be slowed drastically by the thermally excited electrons. In combination with the fundamental criteria, with $E_{p,O} > \Delta E_{e,g} \gg k_B T_c$. Limited materials satisfy $E_{p,O} > 5k_B T$ at room temperature, where $5k_B T = 130$ meV. The most energetic optical-phonon mode in a typical semiconductor is less energetic than 80 meV, as indicated in Fig. 13 [12]. Only the first-row elements are light enough, forming bonds strong enough to enable optical phonons more energetic than 130 meV. Diamond and cubic BN, for example, have optical-phonon cutoff energies of around 160 meV. The bandgap and optical-phonon energy are, therefore, correlated; however, $\Delta E_{e,g} \gg E_{p,O}$ in most materials. While $\Delta E_{e,g} \approx E_{p,O}$ is achievable in soft materials with a metal-semimetal-semiconductor transition, such as $\text{Hg}_x\text{Cd}_{1-x}\text{Te}$ (mercury cadmium telluride (MCT)), these semimetals hold extremely weak bonds, and exhibit optical phonons with $E_{p,O} < 25$ meV.

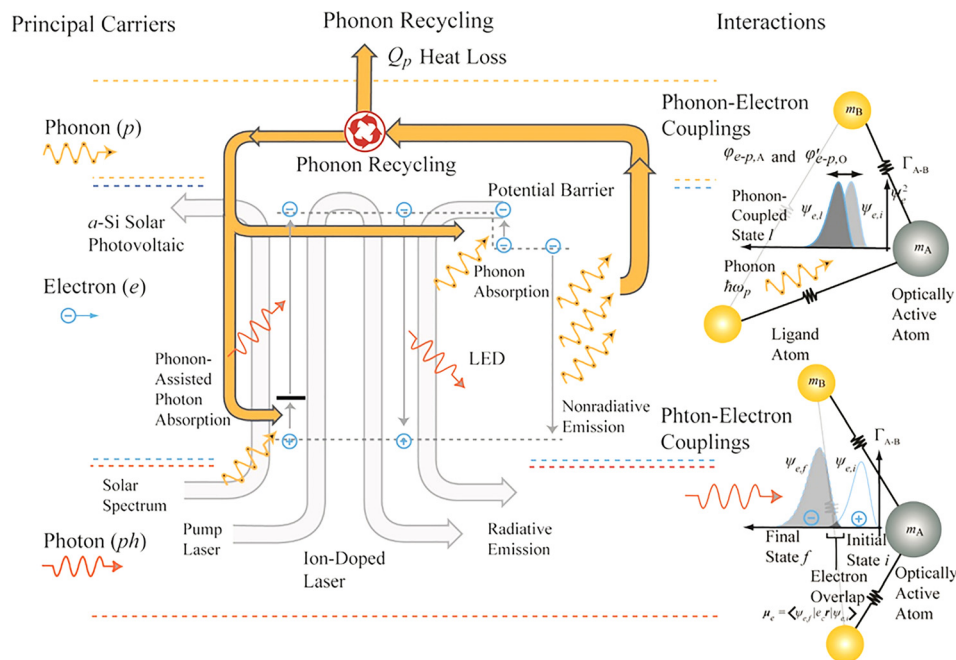


Fig. 9 Phonon recycling introduced in photonic energy-conversion systems

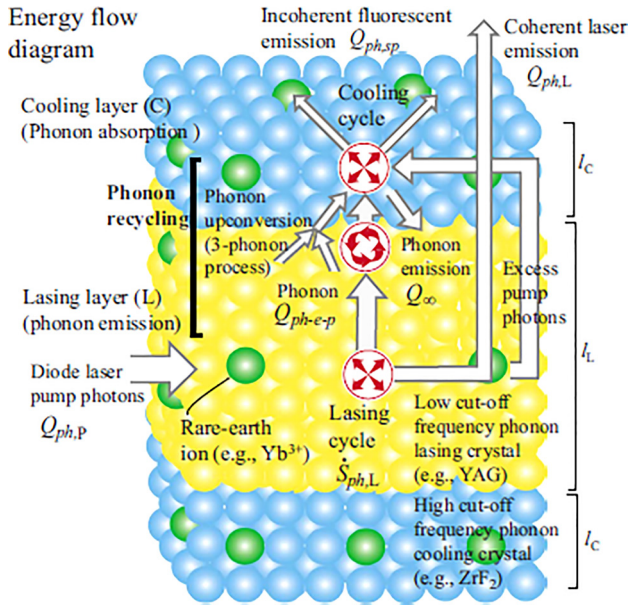


Fig. 10 Phonon recycling in ion-doped laser layer and its adjacent cooling layers [8]. Copyright 2009 by American Institute of Physics.

An efficient pV requires $E_{p,O} > \Delta E_{e,g} \gg k_B T$, as in tuned graphene. In typical materials at 300 K, however, $\Delta E_{e,g} \gg E_{p,O}$ or $E_{p,O} \approx k_B T$, as the strong bonds, enabling energetic phonon modes, also localize electrons while opening a large bandgap. The symmetry of group IV, sp^2 coordinated materials (such as graphene) enables them to overcome this trend [12].

6.3 Phonovoltaic Performance of Graphene. Graphene is a notable exception: It has 200 meV optical-phonon modes and an electronic structure that can be tuned from its semimetallic state (pure graphene) to a semiconductive state. Its sp^2 hybridized carbon-carbon bonds (Fig. 14) induce the extremely energetic optical-phonon modes, while the hybridization and the crystal symmetry also allow for the fourth, p -bound electrons to move freely through the crystal, creating the semimetallic state. Both symmetry and hybridization are crucial. For example, hexagonal

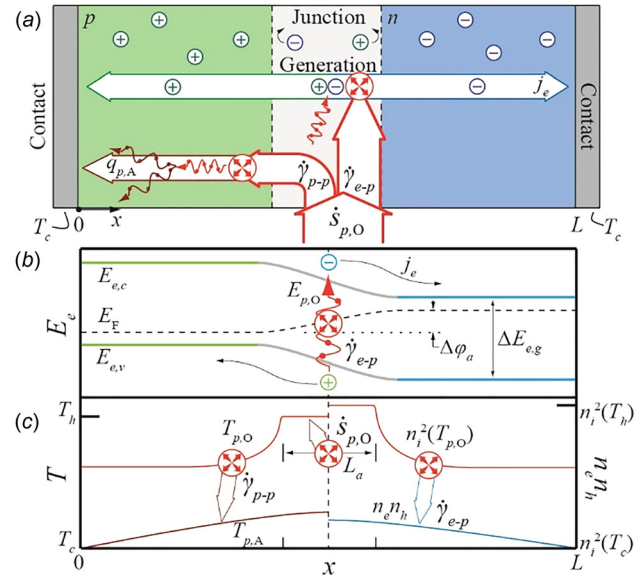


Fig. 12 (a) The phonovoltaic cell; (b) its generation of entropy and power; (c) the resulting efficiency limit [13–15]. Copyright 2019 by American Institute of Physics.

boron nitride (h-BN) exhibits more energetic optical-phonon modes and a less energetic bandgap than the sp^3 hybridized cubic boron nitride. It still exhibits a large bandgap as the p -bound electrons strongly prefer to reside in orbitals, surrounding the more electronegative nitrogen atoms. In addition to having energetic optical-phonon modes and no bandgap, graphene is well suited for use in a phonovoltaic cell for two crucial reasons. First, a bandgap can be opened and tuned in the graphene.

The first Brillouin zone (BZ) of the hexagonal lattice is also indicated in the figure. The graphene:BN structure demonstrates the disordered $[h-C_x(BN)_{y,d}]$ and ordered $[h-C_x(BN)_{y,o}]$ BN doping of graphene. In the ordered scheme, the B and N atoms replace carbon atoms in diverse sublattices (SL), such as B replaces SL 1 carbon atoms while N replaces SL 2 carbon atoms. In the disordered scheme, the B and N atoms are spread to both sublattices [12].

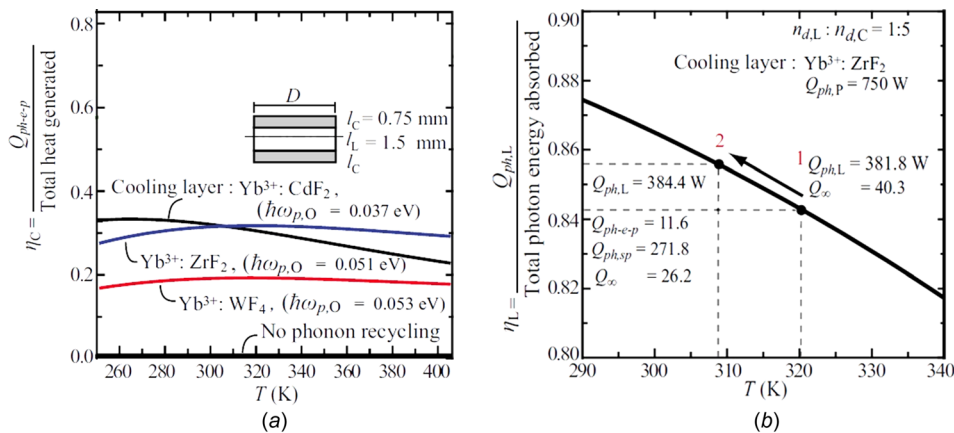


Fig. 11 (a) Phonon-cooling performance as a function of temperature for phonon-recycled ion-doped laser by employing three different cooling crystals $D = 1$ cm, $l_L = 1.5$ mm, and $l_C = 0.75$ mm, Yb^{3+} doped disk is used, and emission spectra of Yb^{3+} : ZBLANP is used to calculate the spontaneous emission peak of anti-Stokes cooling. The second law limit of the anti-Stokes cooling is also shown; (b) Laser operation conditions as a function of temperature with (2) and without (1) phonon recycling. The reduced cooling load corresponds to a reduced laser crystal temperature and moves the operating condition to 2 [8]. Copyright 2009 by American Institute of Physics.

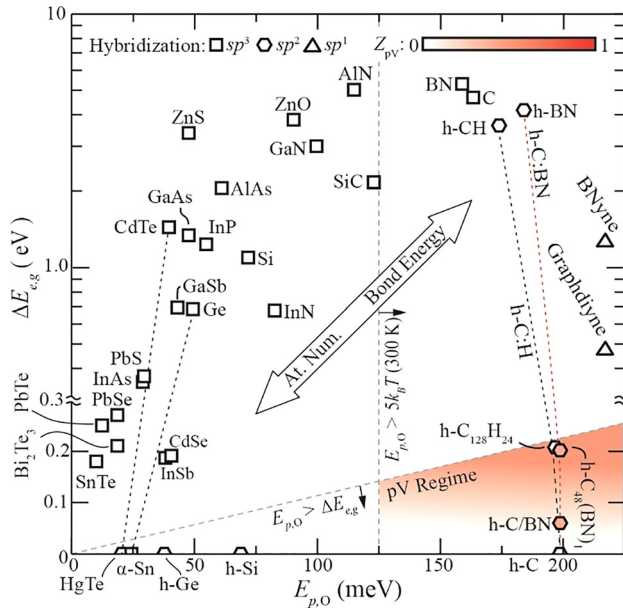


Fig. 13 The bandgap and optical-phonon energy of various semiconductors [15]

The resulting phonovoltaic efficiency η_{pV} , which is roughly proportional to the Carnot limit, and η_{pV}/η_C , are presented in Fig. 15 [12]. The hydrogenated graphene cannot succeed as a phonovoltaic material. This is attributable to its negligible interband electron-phonon coupling. In contrast, the electron-phonon coupling in graphene: BN does not depend on the BN concentration. The coupling is weakened slightly, limiting $\gamma_{e-p}^* < 0.75$. In combination, this limits the figure of merit to $Z_{pV} < 0.6$. This still enables photoelectricity generation with an efficiency of up to $0.5\eta_C$. The bilayer graphene under a cross-plane field avoids both these concerns. The electronic density of states increases near the band edge, such that γ_{e-p}^* increases as $\Delta E_{e,g}$ approached $E_{p,O}$. This indicates the phonovoltaic figure of merit can reach 0.9.

The former two both reached substantial figures of merit, enabling efficiency photoelectric power generation [12].

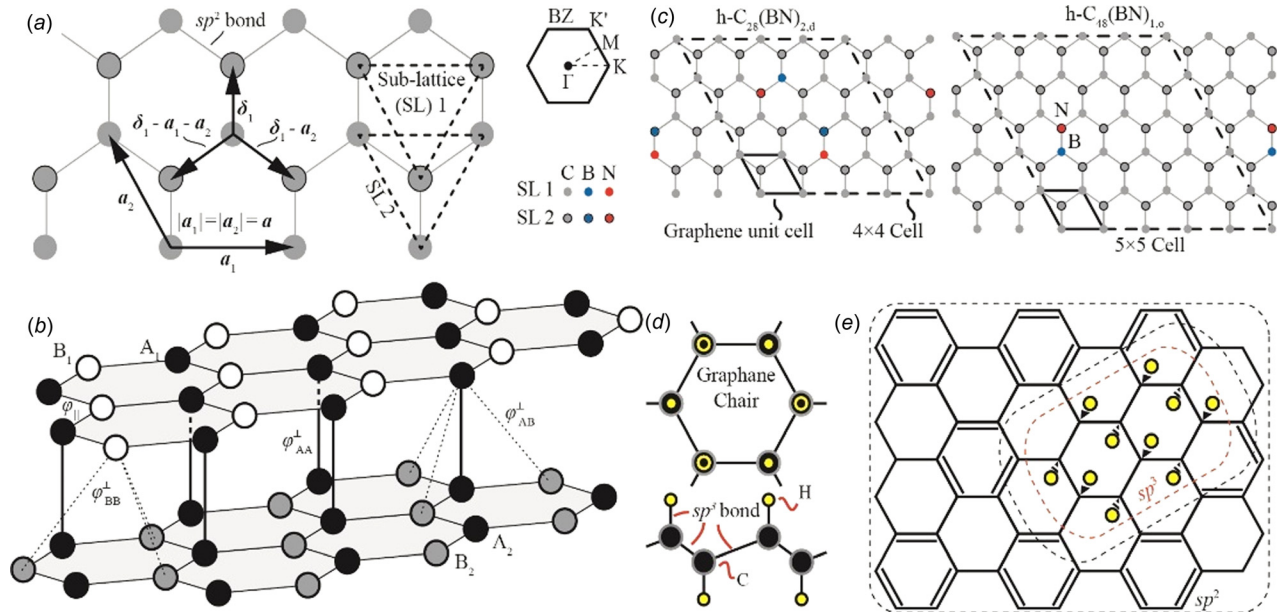


Fig. 14 Structure of (a) graphene; (b) bilayer graphene; (c) graphene: BN, and (d) fully and (e) partially hydrogenated graphene in the chair configuration [15]. Copyright 2019 by American Institute of Physics.

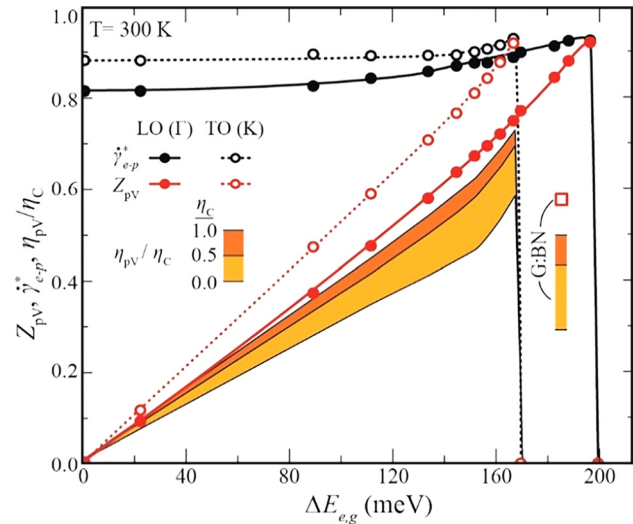


Fig. 15 The phonovoltaic performance, pV figure of merit, dimensionless γ_{e-p}^* , ratio of pV efficiency to the Carnot efficiency η_C as a function of bandgap energy for bilayer graphene under a cross-plane field, graphene: BN (G: BN), and graphene: H(G: H) [15]. Copyright 2019 by American Institute of Physics.

7 Fission Energy Cascade: Nonequilibrium Electron-Phonon Coupling

Energy conversion from a chemical bond, nuclear fission, or solar radiation to heat, first leads to the excitation of intermediary carriers into a nonequilibrium occupancy, and gradually to equilibrium sensible heat (temperature) gain. Energy cascades from the initial low-entropy, high-energy state into high-entropy, low-energy heat. The fission energy cascade mentioned in Fig. 1 is displayed in Fig. 16, with the energy conversion and increase in the entropy (time) [3,9]. The primary mechanism in the conversion of fission energy to heat is the electron cascade. Herein a substantial number of initial delta-rays are formed as the fission fragments ionize the fuel. These energetic electrons subsequently cause further ionization events, producing a secondary collection of delta-rays (which can themselves create tertiary electrons) within a few fs.

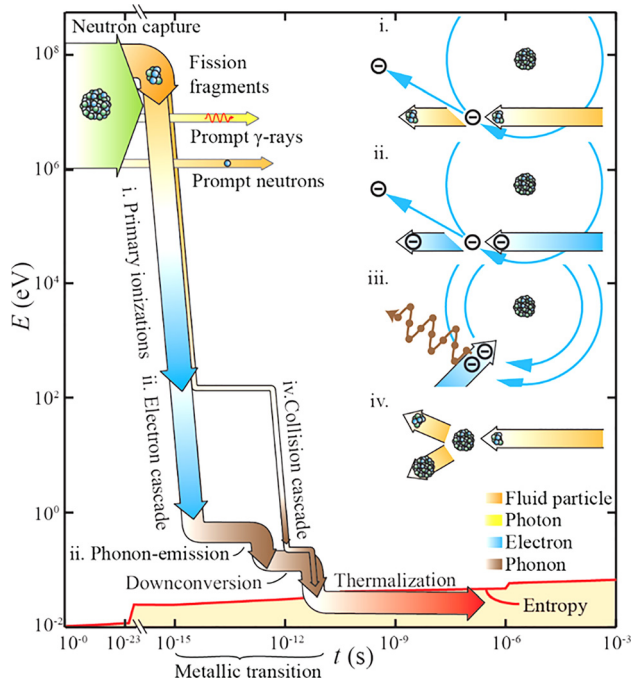


Fig. 16 Evolution in the fission energy conversion to heat, the products, and their fates and increase in the entropy of the system, as thermalization is reached [5,11]

The excited electron system eventually relaxes through electron-phonon, electron-defect, and electron-photon interactions, within a few ps.

The UO_2 compression (attributable to an increase in temperature) metallization occurs within a few ps. Fission involves phonon, electron, fluid particle (energetic traveling ions), and photon (γ -rays) [3,9].

7.1 Energy Cascade of Electronic Stoppage of Penetrating Fission Products and Electronic Heating of Lattice. This process disrupts the atomic lattice of the material. Atomic collisions, therefore, create defects. The electron plasma (formed by the electron cascades) deposits a massive energy quantity into the phonon system as it cools. This leads to local melting and atomic ejections along the path of the fission fragment, as indicated in Fig. 17. The accumulation of defects and melted regions degrades the integrity of the nuclear fuel over time while the melted region partially recovers. Predicting the extent of the damage to the fuel, understanding the mechanisms through which this damage occurs, and creating strategies for damage mitigation or recovery, are of interest in material science and nuclear engineering.

This process may induce metallization along the ion track. The lattice is partially recovered around the ion track radius R_t [9].

7.2 Metallization of UO_2 Caused by Nonequilibrium Energized Electrons. Based on its chemical composition, it is to be expected that UO_2 is a metal with its two unbound electrons partially filling the f -bands. The strong correlation among the f -band electrons in UO_2 , however, opens a substantial bandgap between the two occupied f -bands and the remaining, unoccupied f -bands. Conversely, UO_2 is a Mott insulator. This strong correlation precludes the accurate simulation of UO_2 by employing traditional density-functional theory (DFT) methods, using the local density or general gradient approximations of the exact, Hartree-Fock (HF) exchange-correlation, and functional [9]. Extensions of DFT are employed to simulate UO_2 successfully.

These include the DFT+U, the DFT (local density approximations) + DMFT, and the DFT with the hybrid functional methods. A hybrid functional approach is employed; the meta-GG

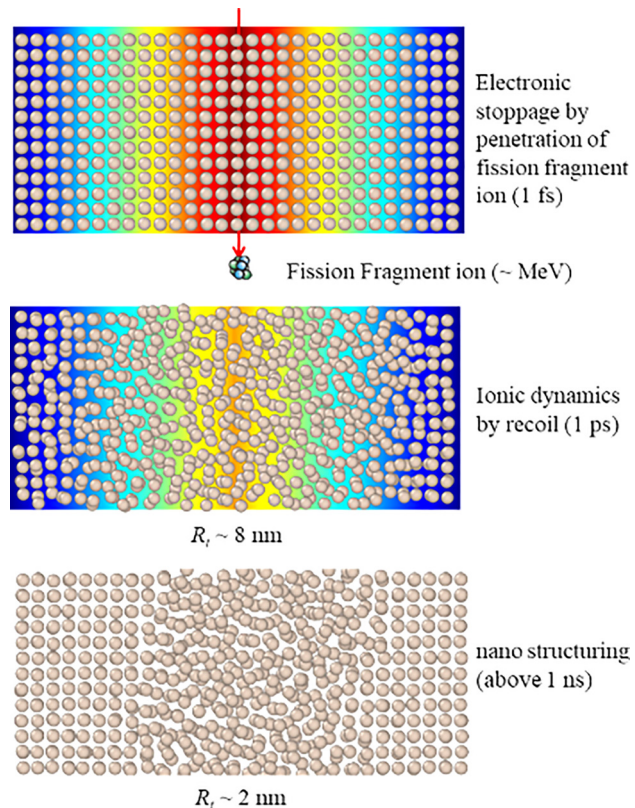


Fig. 17 The energy cascade following the electronic stoppage of a fission fragment energy in bulk UO_2 . Through stoppage by bound electrons, the ion energy is first transferred to the electron system, which causes lattice distortion, ion ejection, and melting [11]. Copyright 2018 by Elsevier.

functional and HF functional are combined to capture the correlation effects. The Heyd-Scuseria-Ernzerhof (HSE) exchange-correlation is employed. This method combines the screened, short-range HF exchange and the short-range Perdew-Burke-Ernzerhof (PBE, a meta-general gradient approximations functional) exchange functional. This mixture is combined with the long-range PBE exchange and complete PBE correlation functionals. The standard HSE06 parameterization indicated to work well for the actinides, including UO_2 , is employed [9].

The electronic properties are calculated by employing the ab initio simulation code Quantum-Espresso Code. The wave functions are modeled by employing a plane-wave basis set with a kinetic energy cutoff of 120 Ry. Scalar relativistic, norm-conserving Martins-Toullier pseudo-potentials are constructed for uranium, configuration $[\text{Rn}]5f^3 6d^1 7s^2$, and oxygen configuration $[\text{He}]2s^2 2p^4$. The simulations are conducted on a $6 \times 6 \times 6$ (6^3) κ_e -mesh with the HF exchange considered on a fully commensurate (6^3) q_e -mesh at each κ_e -point. When evaluating material properties like the density of states, heat capacity, thermal conductivity, or electron-phonon coupling, the resulting mesh of electron eigenvalues is interpolated onto a 30^3 κ_e -mesh. The ground state lattice constant, $a = 5.65 \text{ \AA}$, is established by comparing the crystal energy for variations in a , as shown in Fig. 18. The spin-orbit coupling is not included, as it would reduce the ability to simulate reasonably dense κ_e and q_e -meshes, particularly in the electron-phonon coupling simulations. The physical and electronic properties predicted within the simulations, however, match reasonably well with those recorded in experiments and previously published ab initio calculations.

The energy is offset by the minimum found at $a = 5.65 \text{ \AA}$. The calculated bulk modulus is 181 GPa, reached during the UO_2 compression in the fission product energy cascade [9].

7.3 High Electric Thermal Conductivity of Nonequilibrium UO_2 . The electronic stoppage of charged fission fragments produced during UO_2 fission is relatively well understood; however, the subsequent cascade of energy into the crystal lattice through the electron-phonon coupling is still developing. Recent efforts have explained the cascade by employing the coupled electron and phonon Boltzmann transport equations, indicating the two-temperature model. Tying this model in the classical molecular dynamics simulations of the target lattice, reveal that the electronic system must be metallic to accurately predict the fission fragment track radius.

Impact ionization produces electron shower (primary to tertiary electrons produced by ionizing delta-rays), and UO_2 can also transition to metal under compression. The bond lengths in the molecular dynamic snapshots of the lattice, distorted by ion track, were examined. This demonstrated that this transitional bond-length reduction is met, therefore, inducing local metallic phase under defect. By employing ab initio simulations, stable, compressed UO_2 phases were established. These are metallic within pressures typical of this energy cascade; the electronic, phononic, and electron-phonon coupling properties are evaluated with DFT, and density-functional perturbation theory (DFPT) calculations [9]

$$\dot{\gamma}_{e-p}(E_e) = 1/\langle\tau_e\rangle \approx \sum_{x,y} \langle M_{e-p}^x \rangle^2 D_{e,v}(E_e \pm \hbar\omega_x) [1 - f_e^\circ(E_e \pm \hbar\omega_x)] \left(\frac{1}{2} \mp \frac{1}{2} + f_{p,\alpha}^\circ \right) \quad (7)$$

The electron-phonon coupling (EPC) is provided by the matrix element $M_{e-p}^{ij,\alpha}(\mathbf{\kappa}_e, \mathbf{\kappa}_p)$ describing the scattering of an electron in an initial state $|i, \mathbf{\kappa}_e\rangle$ into a final state $|j, \mathbf{\kappa}_e + \mathbf{\kappa}_p\rangle$ by a phonon with momentum $\mathbf{\kappa}_p$ and polarization α , within perturbation theory is

$$M_{e-p}^{ij,\alpha}(\mathbf{\kappa}_e, \mathbf{\kappa}_p) = \left(\frac{\hbar}{2m\omega_{\alpha,\mathbf{\kappa}_p}} \right)^{1/2} \langle \mathbf{\kappa}_e + \mathbf{\kappa}_p, j | \frac{\partial H_e}{\partial e_{\mathbf{\kappa}_p}^\alpha} | \mathbf{\kappa}_e, i \rangle \quad (8)$$

where H_e is the electron Hamiltonian (the Kohn-Sham potential), m is the average atomic mass, and $\omega_{\alpha,\mathbf{\kappa}}$ and $e_{\mathbf{\kappa}_p}^\alpha$ are the phonon frequency and eigenvector. To calculate these elements, the dynamical matrices describing the phonon eigenproblem and the operator $\partial H_e / \partial e$ are needed. Both are traditionally calculated using the DFPT and a computationally economical alternate limit considers electrons in the same state with the zone-center, phonons, such as $M_{e-p}^{ij,\alpha}(\mathbf{\kappa}_e, \mathbf{\kappa}_p = \Gamma)$. Under this restriction, the approximate can be rewritten as

$$M_{e-p}^{ii,\alpha}(\mathbf{\kappa}_e, \Gamma) = \left(\frac{\hbar}{2m\omega_{\alpha,\Gamma}} \right)^{1/2} \frac{\langle \mathbf{\kappa}_e, i | \delta H_e(\Delta e_{\Gamma}^\alpha) - H_e | \mathbf{\kappa}_e, i \rangle}{\Delta e_{\Gamma}^\alpha} \quad (9)$$

where $\delta H_e(\Delta e_{\Gamma}^\alpha)$ is the electric Hamiltonian when the atoms are displaced by the phonon eigenvector e_{Γ}^α normalized by a distance of Δe_{Γ}^α . Noting that $\langle \mathbf{\kappa}_e, i | \delta H_e(\Delta e_{\Gamma}^\alpha) | \mathbf{\kappa}_e, i \rangle = \delta E_{e,\mathbf{\kappa}_e,i}$ and $\langle \mathbf{\kappa}_e, i | H_e$

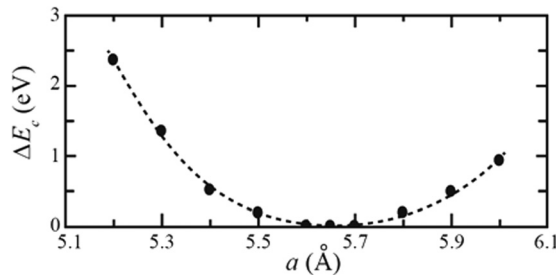


Fig. 18 UO_2 crystal energy for variations in the lattice constant [11]. Copyright 2018 by Elsevier.

$|\mathbf{\kappa}_e, i\rangle = E_{e,\mathbf{\kappa}_e,i}$, the restricted EPC matrix elements can be evaluated through self-consistent DFT-HSE simulations of perturbed and unperturbed UO_2 , respectively. The phonon eigenvectors and frequencies are still required to perturb the atoms, construct $\delta H_e(\Delta e_{\Gamma}^\alpha)$, and evaluate $\delta E_{e,\mathbf{\kappa}_e,i}$ [9].

The electron lifetime is calculated as indicated in Fig. 19(a) as a function of temperature [9]. The electron thermal conductivity is then calculated, and the results are presented in Fig. 19(b) for various nonequilibrium conditions and pressures [9]. As disclosed and as expected, the conductivity depends strongly on the degree of nonequilibrium and the transition of UO_2 from an insulator to a metal. For example, insulative UO_2 has an exceptionally low conductivity until the thermal energy approaches the bandgap, and the conducting states are activated. At elevated temperatures, $T_e > 10,000\text{K}$, insulating UO_2 approaches the thermal conductivity of the highly pressurized, metallic/semimetallic UO_2 .

Even metallic, however, and semimetallic UO_2 hold a relatively low thermal conductivity under equilibrium conditions. Substantial nonequilibrium is required to approach a thermal conductivity above 50W/m-K (required for good agreement between the experiments and TTM+MD simulations). Extreme nonequilibrium is predicted within the TTM+MD simulations. This order of thermal conductivity is, therefore, achievable in pressurized, semimetallic UO_2 (absorption of fission products energy increase temperature and pressure). This causes the electrical insulator to grow into a metal with relatively high electric thermal conductivity. When large thermal conductivity is employed, the predicted fission product energy cascade damage to the lattice matches justly with the experiments [9].

Under equilibrium conditions, the conductivity is suppressed by the short electron lifetime [9].

8 Outlook

From the above atomic-level energy-conversion examples, heat transfer and its control at the quantum-mechanical scale are dominant. They remain central to the understanding and discovery of new energy-conversion efficiency enhancement and devices. This review outlines several solid-state heat-harvesting devices. Recent research led to drastic improvement on this front. Thermophotovoltaics and (photon-enhanced) thermionics are rapidly becoming attractive technologies, eliciting a substantial and renewed

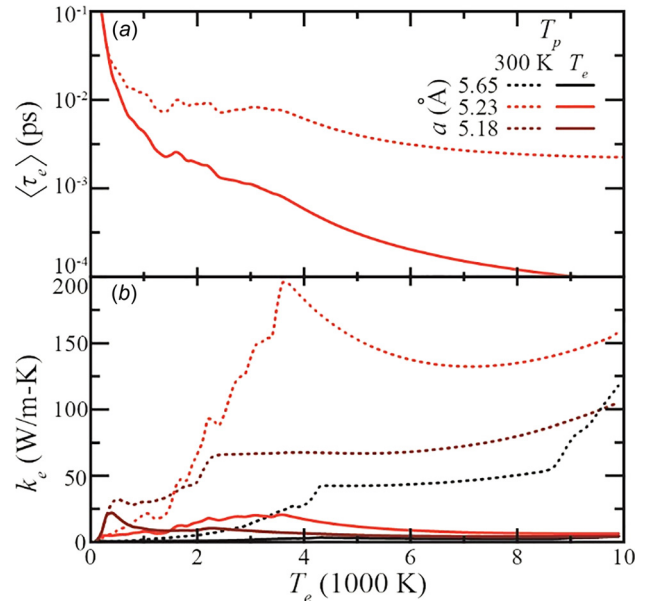


Fig. 19 Electron lifetime (a) and thermal conductivity (b) for variations in the electron temperature and electron-phonon nonequilibrium [11]. Copyright 2018 by Elsevier.

research effort. Concurrently, researchers have substantially improved the record thermoelectric material figure of merit, prospering to an increasingly effective solid-state cooling and waste heat recovering technology. Recently, the first reported laser cooling of a semiconductor was achieved.

The substantial improvements in manufacturing technology motivated these promising efforts were. This allows for the creation of micro- and nanoscale devices and material features in computation power, and the associated condensed matter theory. Much more efficient and informed material and device design can, therefore, occur, accelerating research efforts. Observations from this holistic perspective indicate that thermal electricity is limited by the high entropy of its energy source—heat. It is observed that the successful thermal-electric cycles can overcome this limitation by shaping heat into a less entropic, narrow-spectrum, thermal emission. This includes a narrow spectrum of surface-phonon-polaritons in a thermophotovoltaic or a narrow spectrum of thermionic emission in a photon-enhanced thermionic converter [12].

Both these technologies can reshape the broad-spectrum, black-body radiation of the sun at 5778 K sun into a narrow spectrum of electronic or electromagnetic emissions near 1 eV. This enables heat harvesting at an efficiency approaching 50%. While the Carnot limit of such a cycle is reduced from that of the sun to that of the material melting temperature, the benefits drastically outweigh this disadvantage. Phonolectricity, in contrast, intervenes before substantial entropy materializes. This allows a phonolectric device to sustain extreme nonequilibria without melting, as the hot optical-phonon population can be contained in only a few states. It employs a local, rather than spatial, nonequilibrium to drive energy conversion. It can (and likely must), therefore, function as an in situ optical-phonon recycler rather than an ex-situ heat recovery device.

The phonovoltaic cell is the sole example of a phonolectric device, requiring substantially more study. Most importantly, it must be demonstrated experimentally. The likelihood of its success would be greatly increased if nongraphene-based materials were established with a large figure of merit and could be incorporated in 3D devices. Heterostructures could be constructed to enhance the EPC and electron-phonon nonequilibrium. Finally, multiphonon absorption processes may be possible at extreme nonequilibria, which could enable additional material candidates and higher conversion efficiency.

Acknowledgment

It was a privilege to collaborate with inspiring Ph.D. students and colleagues from the University of Michigan *Heat Transfer Physics Laboratory*, contributing to this research-education effort. The work was supported by the U.S. National Science Foundation program on Thermal Transport and Processes (CTS0553651 and CBET 1332807) and the University of Michigan Center for Solar and Thermal Energy-Conversion, an Energy Frontier Research Center funded by the U.S. Department of Energy, Office of Basic Energy Science (Award No. DE-SC-0000957). Computing resources of the U.S. Department of Energy National Energy Research Scientific Computing Center (Office of Science, Contract No. DE-AC02-05CH11231) were employed.

Funding Data

- U.S. National Science Foundation program on Thermal Transport and Processes (CTS0553651 and CBET 1332807; Funder ID: 10.13039/100000146).
- U.S. Department of Energy, Office of Basic Energy Science (Award No. DE-SC-0000957; Funder ID: 10.13039/100006132).
- Computing resources of the U.S. Department of Energy National Energy Research Scientific Computing Center

(Office of Science, Contract No. DE-AC02-05CH11231; Funder ID: 10.13039/100017223).

Nomenclature

a	= lattice constant, Å
A	= acoustic
A	= area, m ²
c_p	= specific heat at constant pressure, J/kg-K
D	= density of states, 1/eV-Å ³
e	= electron
\mathbf{e}	= phonon eigenvector
E	= energy, eV
e_c	= electron charge, C
\mathbf{e}_e	= electric field vector, V/m
EPC	= electron-phonon coupling
f	= fluid particle
f_i	= energy occupancy distribution function
\hbar	= reduced Planck constant, eV-s
H	= Hamiltonian (eV)
j_e	= current density, A/m ²
k	= thermal conductivity, W/m-K
k_B	= Boltzmann constant, eV-K
L	= longitudinal
m	= mass, kg
M	= interaction matrix element
\dot{n}_i	= volumetric generation rate, 1/m ³ -s
O	= optical
p	= phonon
P	= power, W
ph	= photon
pV	= phonovoltaic
pV	= photovoltaic
Q	= heat flow rate, W
\dot{S}_{i-j}	= energy-conversion heat transfer, W
\dot{s}_{i-j}	= volumetric energy-conversion, W/m ³
R_t	= ion track radius, nm
t	= time, s
T	= transverse
T	= temperature, K
u_e	= electron drift velocity, m/s
V	= volume, m ³
Z	= figure of merit
ΔE	= bandgap energy, eV

Subscripts

C	= Carnot
e	= electron
f	= fluid particle
p	= phonon
ph	= photon
pV	= phonovoltaic

Superscripts

O	= equilibrium
*	= dimensionless

Greek Symbols

$\dot{\gamma}_{e-p}$	= electron-phonon interaction rate, 1/s
Δ	= displacement, Å
η	= efficiency
$\boldsymbol{\kappa}$	= wave vector, 1/m
$\boldsymbol{\mu}_{ph-e}$	= transition dipole moment, C-m
τ	= relaxation time, s
φ_e	= electric potential (V)
ω	= angular frequency, rad/s

Others

$\langle \rangle$	= bra-ket notation
-------------------	--------------------

Abbreviations

AIMD = *ab initio* molecular dynamics
BN = boron nitride
BZ = brillouin zone
DFPT = density-functional perturbation theory
DFT = density-functional theory
EPC = electron-phonon coupling
FFT = fast Fourier transform
HF = Hartree–Fock
HPAB = hot-phonon absorption barrier
HSE = Heyd–Scuseria–Ernzerhof
PBE = Perdew–Burke–Ernzerhof
SL = superlattice
SPV = solar photovoltaics
TE = thermoelectric
TI = thermionic
TS = transition state

References

- [1] Kaviany, M., 2011, *Essentials of Heat Transfer*, Cambridge University Press, New York.
- [2] Melnick, C., Kaviany, M., and Kim, M. H., 2013, “Roles of Core-Shell and δ -Ray Kinetics in Layered BN α -Voltaic Efficiency,” *J. Appl. Phys.*, **113**(6), p. 063703.
- [3] Kaviany, M., 2014, *Heat Transfer Physics*, 2nd ed., Cambridge University Press, New York.
- [4] Kern, G., Kresse, G., and Hafner, J., 1999, “Ab Initio Calculation of the Lattice Dynamics and Phase Diagram of Boron Nitride,” *Phys. Rev. B*, **59**(13), pp. 8551–8559.
- [5] Kim, J., Kapoor, A., and Kaviany, M., 2008, “Material Metrics of Laser Cooling of Solids,” *Phys. Rev. B*, **77**(11), p. 115127.
- [6] Kim, J., and Kaviany, M., 2008, “Phonon Recycling in Ion-Doped Lasers,” *Appl. Phys. Lett.*, **95**, p. 074103.
- [7] Kim, J., and Kaviany, M., 2010, “Phonon-Enhanced Absorption of Alloyed Amorphous Silicon for Solar Photovoltaic,” *Phys. Rev. B*, **82**(13), p. 134205.
- [8] Kim, K. N., and Kaviany, M., 2016, “Phonocatalysis. An Ab Initio Simulation Experiment,” *AIP Adv.*, **6**(6), p. 065124.
- [9] Kim, W. K., Melnick, C., Shim, J. H., and Kaviany, M., 2018, “Role of Compression Metallization in UO₂ Fission-Product Energy Cascade Track: Multiscale Electron-Phonon Analyses,” *J. Nucl. Mater.*, **511**, pp. 148–163.
- [10] Melnick, C., and Kaviany, M., 2016, “Phonovoltaic. I. Harvesting Hot Optical Phonons in Nano-p-n Junction,” *Phys. Rev. B*, **93**(9), p. 094302.
- [11] Melnick, C., and Kaviany, M., 2017, “Bilayer Graphene Phonovoltaic-FET: In Situ Phonon Recycling,” *Phys. Rev. B*, **96**(20), p. 205444.
- [12] Melnick, C., and Kaviany, M., 2019, “From Thermoelectricity to Phonoelectricity,” *Appl. Phys. Rev.*, **6**(2), p. 021305.
- [13] Ruan, X. L., and Kaviany, M., 2006, “Enhanced Laser Cooling of Ion-Doped Nanopowders,” *Phys. Rev. B*, **73**(15), p. 155422.
- [14] Ruan, X. L., and Kaviany, M., 2007, “Advances in Laser Cooling of Solids,” *ASME J. Heat Transfer-Trans. ASME*, **129**(1), pp. 3–10.
- [15] Ruan, X. L., and Kaviany, M., 2008, “Ab Initio Photon-Electron and Electron-Vibration Coupling Calculations in Laser Cooling of Ion-Doped Solids,” *J. Comput. Theor. Nanosci.*, **5**(2), pp. 221–229.
- [16] Shin, S. H., Melnick, C., and Kaviany, M., 2013, “Heterobarrier for Converting Hot-Phonon Energy to Electric Potential,” *Phys. Rev. B*, **87**(7), p. 075317.
- [17] Shin, S. H., and Kaviany, M., 2013, “Entropy Production in Hot-Phonon Energy Conversion to Electric Potential,” *J. Appl. Phys.*, **114**(8), p. 083710.
- [18] Shin, S. H., and Kaviany, M., 2015, “Toward Reversing Joule Heating With a Phonon-Absorbing Heterobarrier,” *Phys. Rev. B*, **91**(8), p. 085301.
- [19] Shin, S. H., and Kaviany, M., 2015, “Optical Phonon Production by Upconversion: Heterojunction-Transmitted Versus Native Phonons,” *Phys. Rev. B*, **91**(16), p. 165310.
- [20] Srivastava, G. P., 1990, *The Physics of Phonons*, Adam Hilger, Bristol, UK.
- [21] Adachi, S., 2004, *Handbook on Physical Properties of Semiconductors*, Vol. 2, Springer Science & Business Media, New York.
- [22] Carey, V., Chen, G., Grigoropoulos, C., Kaviany, M., and Majumdar, A., 2008, “A Review of Heat Transfer Physics,” *Nanoscale Microscale Thermophys. Eng.*, **12**(1), pp. 1–60.
- [23] Huang, B. L., and Kaviany, M., 2006, “Structural Metrics of High-Temperature Lattice Conductivity,” *J. Appl. Phys.*, **100**(12), p. 123507.
- [24] Span, G., Wagner, M., Grasser, T., and Holmgren, L., 2007, “Miniaturized Teg With Thermal Generation of Free Carriers,” *Phys. Status Solidi (RRL)*, **1**(6), pp. 241–243.